Patched Green's function techniques for two-dimensional systems: Electronic behavior of bubbles and perforations in graphene

Mikkel Settnes,[*] Stephen R. Power, Jun Lin, Dirch H. Petersen, and Antti-Pekka Jauho
Center for Nanostructured Graphene (CNG), DTU Nanotech, Technical University of Denmark, DK-2800 Kongens Lyngby, Denmark

We present a numerically efficient technique to evaluate the Green's function for extended two-dimensional systems without relying on periodic boundary conditions. Different regions of interest, or "patches," are connected using self-energy terms which encode the information of the extended parts of the system. The calculation scheme uses a combination of analytic expressions for the Green's function of infinite pristine systems and an adaptive recursive Green's function technique for the patches. The method allows for an efficient calculation of both local electronic and transport properties, as well as the inclusion of multiple probes in arbitrary geometries embedded in extended samples. We apply the patched Green's function method to evaluate the local densities of states and transmission properties of graphene systems with two kinds of deviations from the pristine structure: bubbles and perforations with characteristic dimensions of the order of 10–25 nm, i.e., including hundreds of thousands of atoms. The strain field induced by a bubble is treated beyond an effective Dirac model, and we demonstrate the existence of both Friedel-type oscillations arising from the edges of the bubble, as well as pseudo-Landau levels related to the pseudomagnetic field induced by the nonuniform strain. Second, we compute the transport properties of a large perforation with atomic positions extracted from a transmission electron microscope image and show that current vortices may form near the zigzag segments of the perforation.

I. INTRODUCTION

Following the isolation of graphene a general class of two-dimensional materials with widely diverse and unique electrical, mechanical, and optical properties has been realized [1,2]. Two-dimensional materials are almost entirely surface and are therefore very susceptible to external influences like direct patterning, [3,4] adsorbate atoms, [5] strain [6], etc. This variety of ways to alter and control the material properties opens a huge range of engineering possibilities [7]. In this context, it becomes important to investigate large-scale disorder or patterning in relation to the electronic properties of graphene and related two-dimensional materials. From a theoretical perspective, several methods are available [8]. Typically, the electronic structure of the system is described with a tight-binding-type Hamiltonian and a popular approach is then to construct the entire system in a piecewise manner using recursive Green's functions (RGFs) [9]. In this way, we can extract the necessary terms for calculating physical quantities of interest. The RGF method is best suited for systems which are either finite or periodic in one dimension. It is frequently used for modeling transport, where self-energies calculated using recursive techniques are used to attach semi-infinite pristine leads to either side of a finite device region [10]. Alternatively, an efficient approach to large disordered systems is the real-space Kubo-Greenwood approach [11]. However, this method cannot include open boundary conditions and can only obtain average system quantities, as opposed to local electronic and transport properties.

In the most common formulation, the RGF method treats (quasi) one-dimensional systems with only two leads. Although variants of the method can be used for arbitrary geometries and multiple leads [12–14], the method remains limited to finite-width or periodic systems. Consequently, it cannot describe local and nonperiodic perturbations, or pointlike probes similar to those considered experimentally [15–17]. An extension of recursive techniques, to allow efficient treatment of local properties in systems without periodicity or finite sizes, would allow for easier theoretical investigation of systems which are computationally very expensive, or completely out of reach, using existing methods.

In this paper, we develop a Green's function (GF) method which is able to efficiently treat large and finite-sized "patches" embedded in an extended system, as shown in Fig. 1. The method combines an analytical formulation of the GFs describing a pristine system [18,19] with an adaptive RGF method to describe the patches. It allows for calculation of both local electronic and transport properties and for the inclusion of multiple leads and arbitrary geometries embedded within an extended sample.

This patched GF method exploits an efficient calculation of the GF for an infinite pristine system using complex contour techniques. Using this GF, an open-boundary self-energy term can be included in the device Hamiltonian to describe its connection to an extended sample. The device region itself, containing nanostructures, (non)uniform magnetic fields, and/or leads, is then treated with an adaptive recursive method. We demonstrate the formulation using graphene, but it is generally applicable to all (quasi) two-dimensional structures where the GF for the infinite pristine system can be determined. Consequently, the patched GF method is a versatile tool for efficient investigation of nonperiodic nanostructures in extended two-dimensional systems.

The rest of the paper is outlined as follows. The general formalism is developed in Sec. II A by calculating the open boundary self-energy from the pristine GF. In Sec. II B we use graphene as an example to show the calculation of the pristine GF, while Sec. II C discusses the adaptive recursive method used to treat the device when including the boundary
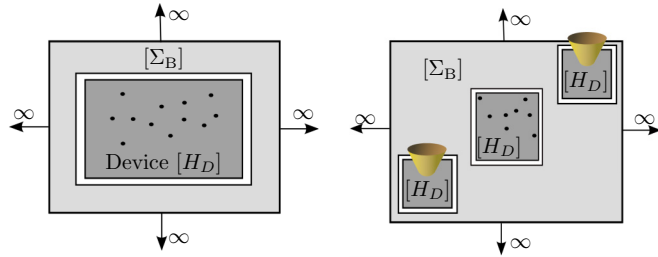
---

*mikse@nanotech.dtu.dk

FIG. 1. (Color online) The left panel shows a schematic of a computational setup containing a finite device 'patch,' described by H_D, embedded within an extended system described by the self-energy Σ_B. The right panel shows a computational setup containing several device patches of interest.

self-energy. In Sec. III we use the developed method to study the local density of states of a graphene sample under the influence of a local strain field. As a result, we can compare local density of state (LDOS) maps with pseudomagnetic field distributions. In this way, we show the existence of Friedel-type oscillations along with pseudomagnetic field effects in the LDOS. Finally, in Sec. IV, we use the patched GF technique to demonstrate the existence of vortexlike current patterns in the presence of a perforation within an extended graphene sheet.

II. METHOD

We consider the computational setup schematically shown in the left panel of Fig. 1, where a device region is embedded within an extended two-dimensional system. This setup ensures that we are not including edge effects due to the finite-size of the simulation domain [20]. The device region is described by a Hamiltonian, H, which may include disorder, deformations, mean-field terms, (non)uniform magnetic fields or leads, etc. This device region is embedded into an extended system by applying a self-energy term, Σ_B. To consider the setup in Fig. 1, we need two things. First, we need to construct Σ_B to describe the extended part of the system and, second, we need an efficient way to describe the device region while taking Σ_B into account. Furthermore, the treatment of the device

should be able to consider arbitrary geometries, including mutually disconnected patches within the extended system, as shown in the right panel of Fig. 1.

We describe the method in three steps:

(A) derivation of the boundary self-energy term, Σ_B, in terms of the pristine lattice GFs;

(B) calculation of the real-space GF needed in the self-energy calculation. (we use graphene as an example);

(C) implementation of an adaptive RGF method to build the device region(s) efficiently while including the self-energy term(s) Σ_B.

A. Boundary self-energy

To construct the boundary self-energy describing the extended region in Fig. 1, we consider the simple graphene example in Fig. 2(a). Here a central device region, indicated by the dashed square, is embedded in an extended sheet. In this example both the extended area and the device region are assumed to be graphene based, but the following arguments are general to any two-dimensional material. We consider a division of the system into two parts: sites in the device (D) or sites in the extended sheet region. Furthermore, we subdivide the extended sheet into boundary sites (B), which are indicated by blue in Fig. 2 and have a nonzero Hamiltonian element coupling them to the device region, or "sheet" sites, which do not couple to the device region. Within a nearest-neighbor tight-binding Hamiltonian, the boundary sites in Fig. 2(a) are shown by blue symbols and have nonzero couplings to the device sites indicated by red symbols. We can now write the Hamiltonian for the entire system, in block matrix form, as

$$H = \begin{pmatrix} H_{D,D} & V_{D,B} & 0 \\ V_{B,D} & H_{B,B} & V_{B,\text{sheet}} \\ 0 & V_{\text{sheet},B} & H_{\text{sheet}} \end{pmatrix}, \qquad (1)$$

where the light shaded part of Eq. (1) represents an infinite Hamiltonian. The connections between device and sheet (i.e., between the red and blue symbol sites) are contained in the off-diagonal blocks $V_{D,B}$ and $V_{B,D}$.
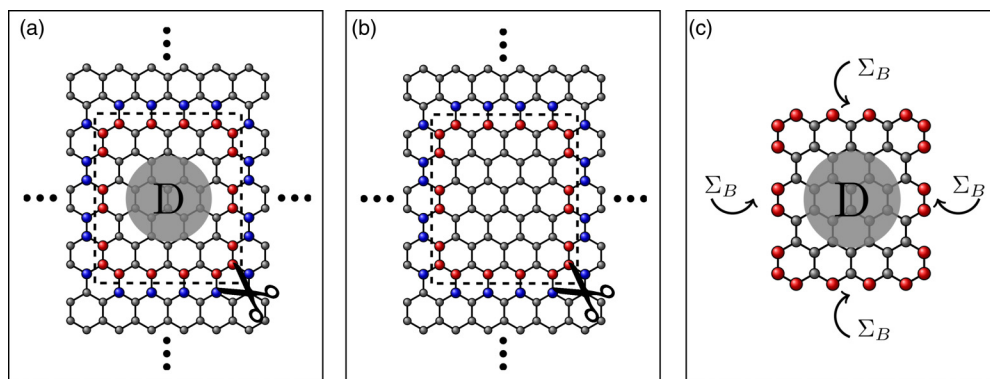

FIG. 2. (Color online) (a) The desired device region, indicated by the dashed square, embedded within an extended system. Red symbols are the edge of the device and blue symbols indicate sites in the surrounding sheet that couples to the device. We obtain the disconnected system discussed in the text by removing the couplings that cross the dashed line. (b) The corresponding pristine system. Again the disconnected system is obtained by removing couplings along the dashed line. (c) How the effect of the extended sheet on the device region is taken into account by the self-energy; see Eq. (4).

We aim to replace the infinite Hamiltonian $\boldsymbol{H}$ with a finite effective Hamiltonian, $\boldsymbol{H}_{\text{eff}} = \boldsymbol{H}_{D,D} + \Sigma_B$, which takes into account the extended sheet using a self-energy term Σ_B. To do this, we consider the *connected* system in panel (a) of Fig. 2 and a disconnected system formed by removing the Hamiltonian elements $\boldsymbol{V}_{D,B}$ and $\boldsymbol{V}_{B,D}$, corresponding to removing couplings crossing the dashed line in Fig. 2(a). The GFs of the connected ($\boldsymbol{G}^{(\text{con})}$) and disconnected ($\boldsymbol{G}^{(\text{dis})}$) systems can be related via the Dyson equation, and in particular we can write the GF of the connected device region as

$$\boldsymbol{G}_{D,D}^{(\text{con})} = \boldsymbol{G}_{D,D}^{(\text{dis})} + \boldsymbol{G}_{D,D}^{(\text{dis})} \boldsymbol{V}_{D,B} \boldsymbol{G}_{B,D}^{(\text{con})}. \tag{2}$$

Applying the Dyson equation again to obtain $\boldsymbol{G}_{B,D}^{(\text{con})}$ and inserting this into Eq. (2) allows us to simplify

$$\boldsymbol{G}_{D,D}^{(\text{con})} = (E\mathbf{1} - \boldsymbol{H}_{D,D} - \Sigma_B)^{-1}, \tag{3}$$

where the self-energy term is given by

$$\Sigma_B = \boldsymbol{V}_{D,B} \boldsymbol{G}_{B,B}^{(\text{dis})} \boldsymbol{V}_{B,D}. \tag{4}$$

We note that the self-energy in Eq. (4) is independent of the considered device and depends only on GF matrix elements connecting sites in the pristine surrounding "frame" that remains when the device is removed from the full system. We take advantage of this to temporarily replace the device with a corresponding pristine region of the same size, as shown in panel (b) of Fig. 2. The self-energy required to incorporate the finite pristine region into an infinite, pristine sheet is the same self-energy, Σ_B, that is required in Eq. (3). We can therefore write the required GF matrix, $\boldsymbol{G}_{B,B}^{(\text{dis})}$, in terms of the GF of the infinite pristine sheet, $\boldsymbol{G}^{(0)}$. These are related using the Dyson equation with a perturbation $-\boldsymbol{V}_{D,B}$,

$$\boldsymbol{G}_{B,B}^{(\text{dis})} = \left(\mathbf{1} + \boldsymbol{G}_{B,D}^{(0)} \boldsymbol{V}_{D,B}\right)^{-1} \boldsymbol{G}_{B,B}^{(0)}. \tag{5}$$

The advantage of writing the self-energy in terms of the pristine sheet GFs, $\boldsymbol{G}_{B,B}^{(0)}$ and $\boldsymbol{G}_{B,D}^{(0)}$, becomes clear in the next section, where we demonstrate an efficient method to calculate these two terms. It is worth noting that $\boldsymbol{G}_{B,D}^{(0)}$ only needs to be calculated for the sites in D which connect to sites in B. These sites are indicated by red in Fig. 2 and are where the self-energy terms need to be added, as shown in panel (c). In this way, the computations only involve matrices corresponding to the edge of the device and not the size of the full device region as straightforward inversion would require.

The calculation scheme can be summarized as follows.

(1) Calculate $\boldsymbol{G}_{B,B}^{(0)}$ and $\boldsymbol{G}_{B,D}^{(0)}$ using the methods outlined in Sec. II B.

(2) Calculate Σ_B from Eqs. (4) and (5).

(3) The finite GF for the device region, $\boldsymbol{G}_{D,D}^{(\text{con})}$, is given by Eq. (3) and can be treated using an adaptive RGF method; see Sec. II C.

We note that this approach does not require a specific geometric shape of the device, nor does the device region need to be contiguous. We can treat different nonconnected patches in an extended system, as shown in the right panel of Fig. 1, by extending the set D to include sites inside each patch and similarly expanding B to include sites at the boundary of each patch. The method presented in this section is applicable to any system where the connected, pristine GFs

are easily obtainable, as demonstrated in the next section using a tight-binding description of graphene as an example.

B. Real-space graphene Green's function

We now turn to the calculation of the real-space GF of the pristine system, which is needed to calculate the self-energy, Σ_B, in Eqs. (4) and (5). The approach required to calculate this quantity is demonstrated below for the case of a graphene sheet described with a nearest-neighbor tight-binding Hamiltonian, but is easily generalized for other cases.

This Hamiltonian is given by

$$\boldsymbol{H} = \sum_{\{i,j\}} t \hat{c}_i^\dagger \hat{c}_j, \tag{6}$$

where the sum $\{i,j\}$ runs over all nearest-neighbor pairs and the carbon-carbon hopping integral is $t \approx -2.7$ eV. The graphene hexagonal lattice can be split into two triangular sublattices, which we denote A and B, and neighboring sites reside on opposite sublattices to each other. Using Bloch functions, the Hamiltonian can be rewritten in reciprocal space as [8]

$$\boldsymbol{H}_{\boldsymbol{k}} = t \begin{pmatrix} 0 & f(\boldsymbol{k}) \\ f^*(\boldsymbol{k}) & 0 \end{pmatrix}, \tag{7}$$

where the matrix form arises from sublattice indexing within a two-atom unit cell and we have used the definition $f(\boldsymbol{k}) = 1 + e^{i\boldsymbol{k}\cdot\boldsymbol{a}_1} + e^{i\boldsymbol{k}\cdot\boldsymbol{a}_2}$, with the lattice vectors $\boldsymbol{a}_1 = a_0(\sqrt{3},3)/2$ and $\boldsymbol{a}_2 = a_0(-\sqrt{3},3)/2$ and a_0 the carbon-carbon distance. With this definition of the unit vectors we have the armchair direction along the y axis (and zigzag along the x axis).

The eigenenergies and eigenstates of the system are easily obtained from this form of the Hamiltonian, and transforming back to real space allows us to write the desired Green's function between sites i and j as [19,21]

$$G_{ij}^0(z) = \frac{1}{\Omega_{BZ}} \int d^2k \frac{N_{ij}(z,\boldsymbol{k})e^{i\boldsymbol{k}\cdot(\boldsymbol{r}_j - \boldsymbol{r}_i)}}{z^2 - t^2|f(\boldsymbol{k})|^2}, \tag{8}$$

where $z = E + i0^+$ is the energy, Ω_{BZ} is the area of the first Brillouin zone. The position of the unit cell containing site i is denoted by $\boldsymbol{r}_i = m_i \boldsymbol{a}_1 + n_i \boldsymbol{a}_2$, with m_i and n_i being integers. Finally, we use the definition $N_{ij}(z,\boldsymbol{k}) = z$, when i and j are on the same sublattice and $N_{ij}(z,\boldsymbol{k}) = tf(\boldsymbol{k})$ if i is on the A sublattice and j is on the B sublattice and $N_{ij}(z,\boldsymbol{k}) = tf^*(\boldsymbol{k})$ when i is on B and j is on A.

To simplify the notation, we introduce the dimensionless k vectors $k_A = 3k_y a_0/2$ and $k_Z = \sqrt{3}k_x a_0/2$ such that $f(k_A, k_Z) = 1 + 2\cos(k_Z)e^{ik_A}$, and write the separation vector in terms of the lattice vectors $\boldsymbol{r} = \boldsymbol{r}_j - \boldsymbol{r}_i = m\boldsymbol{a}_1 + n\boldsymbol{a}_2$. Inserting this into Eq. (8) gives

$$G^0(z,\boldsymbol{r}) = \frac{1}{2\pi^2} \int dk_A \int dk_Z N_{ij}(z,k_A,k_Z)$$
$$\times \frac{e^{ik_A(m+n)+ik_Z(m-n)}}{z^2 - t^2[1 + 4\cos^2(k_Z) + 4\cos(k_A)\cos(k_Z)]}. \tag{9}$$

Equation (9) can be solved using a two-dimensional numerical integration, but as we require Eq. (9) for each GF element individually, we wish to increase the performance by doing one integration analytically using complex contour techniques.

Following the approach of Ref. [19], we use k_A as a complex variable and consider the poles, q, of the denominator

$$q = \cos^{-1}\left[\frac{\frac{z^2}{t^2} - 1 - 4\cos^2(k_Z)}{4\cos(k_Z)}\right]. \tag{10}$$

The sign of the pole must be selected carefully to ensure that it lies within the integration contour, i.e., $\text{Im}(q) > 0$, for contours in the positive half plane corresponding to the situation $m + n \geqslant 0$. Care must also be taken with the additional phase terms that arise for opposite sublattice GFs.

Using the residue theorem and integrating over a rectangular Brillouin zone, $k_A \in [-\pi; \pi]$ and $k_Z \in [-\pi/2; \pi/2]$, we finally reduce Eq. (9) to

$$G^0(z, \boldsymbol{r}) = \frac{i}{4\pi t^2} \int_{-\frac{\pi}{2}}^{\frac{\pi}{2}} dk_Z \frac{N_{ij}(z, q, k_Z) e^{iq(m+n) + ik_Z(m-n)}}{\cos(k_Z)\sin(q)}, \tag{11}$$

with q given by Eq. (10). A similar expression to Eq. (11) can be derived when using k_Z as first integration variable [19]. The above derivation is based upon a nearest-neighbor model, but can be generalized to include, for example, second-nearest-neighbor terms [22], uniaxial strains [23], or any form of rescaled graphene models [24].

We can now use Eq. (11) to calculate the elements of the required GFs, $\boldsymbol{G}_{B,B}^{(0)}$ and $\boldsymbol{G}_{B,D}^{(0)}$, defined in Sec. II A. In this way, Eq. (11) can be used to fill up the elements of the desired matrices one at a time. Since we need GF matrices of size $N_B \times N_B$ and $N_B \times N_D$, where N_D and N_B are the number of sites at the edge of the device region and in the region B, respectively, it could seem very ineffective to calculate one element at a time. However, the total number of GF elements to be calculated is greatly reduced by the symmetries of the pristine graphene lattice. The lattice itself is 6-fold symmetric and each of these 6 identical wedges is, in turn, mirror symmetric, resulting in a 12-fold degeneracy of the GFs indexed by site separation vectors. Additionally, many of the required elements in $\boldsymbol{G}_{B,B}^{(0)}$ and $\boldsymbol{G}_{B,D}^{(0)}$ are identical. For instance, the on-site and nearest-neighbor GF element appear many times, but only need to be calculated once. Taking the device region in Fig. 2 as an example we have $N_D = N_B = 20$, yielding 400 individual elements for a brute-force calculation. Instead, using symmetries and duplicates, we only need to calculate 38 and 42 elements when determining

$\boldsymbol{G}_{B,B}^{(\text{con})}$ and $\boldsymbol{G}_{B,D}^{(\text{con})}$, respectively. The reduction becomes more significant for larger systems, as we generally only need to add the GF elements corresponding to the longest couplings. Consequently, only a small percentage of the GF elements need to be calculated individually and their values for frequently used separations and energies can be stored or reused to enable extremely fast calculation of the required self-energies.

C. Adaptive recursion for device region

In this section we consider the device region where the boundary self-energy can be added at the edge. The full GF of the device region is given by $\boldsymbol{G}_D = (E\boldsymbol{1} - \boldsymbol{H}_D - \Sigma_B)^{-1}$, where we have simplified the notation from Eq. (3). From this GF both transport and local properties can be obtained. However, for most purposes we do not require every element of the GF matrix element in the device region, and so to avoid a time-consuming, full-matrix inversion, various recursive or other decomposition methods are often applied [9,14,20,25–32].

This section outlines an adaptive recursion method which efficiently includes the boundary self-energy as well as an arbitrary device region shape and configuration (and number) of leads. Alternative approaches have been developed to treat arbitrarily shaped regions with multiple leads [12,13,30]. These so-called knitting algorithms add single sites at a time. They rely on a complicated categorizing of sites into different intermediate updating blocks, making the theory and implementation cumbersome. Hence, we use an approach similar to the ones in Refs. [25–27] and employ an adaptive partitioning of the Hamiltonian matrix in order to bring it into the desired tridiagonal form suitable for recursive methods.

Calculating physical properties generally requires certain GFs connecting a specific set of sites in the device region. These sites of interest, for example, could be sites where we want to introduce defects, or couple to probes for transport calculations, or measure properties like the LDOS. We focus first on the general partitioning process and then demonstrate how it can be quickly modified to account for the edge self-energy terms. We begin by placing all these sites of interest into recursive cell 1, as shown by the red sites in Fig. 3. We emphasize that the cells in this process are not of a fixed size and may consist of arbitrary sites which are not necessarily connected. Cell 2 is determined by selecting all the remaining
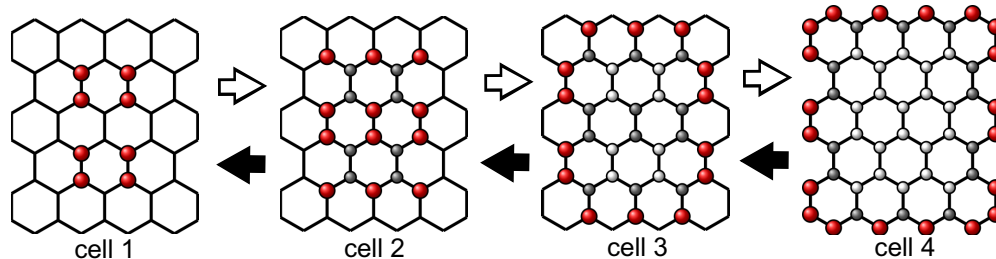

FIG. 3. (Color online) The partitioning of a small graphene sample where all sites of interest are located in cell 1. Cell 2 contains all the sites coupling to cell 1 but which are not themselves part of cell 1. Likewise, cell 3 comprises the sites coupling to cell 2, and so on. The red sites are assigned to the current cell and the lines indicate the sites still to be assigned. The previous cell and all sites already added are indicated by gray and white, respectively. The recursive sweep starting at the final cell and ending in cell 1, indicated by black arrows, gives the GFs connecting all sites of interest. We can also employ a second recursive sweep, as indicated by the white arrows, to obtain local properties everywhere within the device region.

unpartitioned sites which couple directly to sites in cell 1 via a nonzero Hamiltonian matrix element. In the example in Fig. 3, this consists of nearest-neighbor sites of those in cell 1, which are not themselves in cell 1. This process is repeated until all sites in the device region have been allocated a cell and is demonstrated schematically in the panels of Fig. 3, where red sites indicate the current cell and dark gray or white sites indicate sites added to the previous cell or to earlier cells, respectively.

With the resultant block tridiagonal Hamiltonian, we can now employ the usual recursive algorithm, starting from cell $n = N$, so that the final step yields the required GF sites in cell $n = 1$. These terms can then be used to calculate observable quantities like transmission, LDOS, etc. Afterwards a reverse recursive sweep from $n = 1$ to $n = N$ can be implemented to efficiently map local quantities like bond currents or LDOS everywhere within the device region [9]. For completeness the full recursive method is summarized in Appendix A including the reverse sweep. We emphasize that the presented method is not unique to graphene systems, but can be employed to arbitrary tight-binding-like models.

The method offers increased flexibility compared to the standard left-right recursive approach [9], but keeps the operation count scaling $N_{cell} \times M^3$, where N_{cell} is the number of cells and M is the number of sites in each cell. We note that the cell-size fluctuation is greater within the adaptive approach, so that the total operation count will also be higher by a factor dependent on the device aspect ratio and circumference. However, the larger number of matrix elements returned allow the system to be connected to multiple probes or as a patch in an extended system, options not available using a standard recursive sweep. The use of multiple patches within our framework, as illustrated in Fig. 1, can also significantly reduce the percentage of the system that needs to be built recursively. This removes the need for computationally expensive buffer zones, or k-space averaging techniques, that standard RGF techniques would require in attempting calculations of similar systems.

Including the boundary self-energy

We now return to the specific case at hand where the recursive method outlined above needs to be adapted carefully to take account of the boundary self-energy. In general, Σ_B is a non-Hermitian dense matrix connecting all edge sites of the device region. Therefore, it is essential to assign all edge sites to the same cell. This principle is shown in Fig. 4. If cell

$n - 1$ contains sites which connect to an edge site, then cell n must contain not only the edge sites directly connecting to cell $n - 1$, but also all other edge sites, as these are connected to each other via Σ_B. In this way, the cell, $n + 1$, must then contain all the sites connecting to cell n, i.e., also connecting to the edge, but not included in cell n. The full cell partitioning algorithm, including this step, is given in Appendix A.

III. INHOMOGENEOUS STRAIN FIELDS IN GRAPHENE BUBBLES

In this section, we employ the patched GF method to a locally strained graphene system, demonstrating how it can prove to be a useful tool in investigating local properties of nonperiodic nanostructures in extended two-dimensional systems.

Strain engineering has been proposed as a method to manipulate the electronic, optical, and magnetic properties of graphene [23,33–46]. It is based on the close relation between the structural and electronic properties of graphene. The application of strain can lead to effects like band-gap formation [47], transport gaps [33], and pseudomagnetic fields (PMFs) [34–36].

Uniaxial or isotropic strain will not produce PMFs, although it has been shown to shift the Dirac cone of graphene and induce additional features in the Raman signal [48]. On the other hand, inhomogeneous strain fields can introduce PMFs. In this case, the altered tight-binding hoppings mimic the role of a gauge field in the low-energy effective Dirac model of graphene [49,50]. For example, Guinea *et al.* [34] demonstrated that nearly homogeneous PMFs can be generated by applying triaxial strain. One of the most striking consequences of homogeneous PMFs is the appearance of a Landau-like quantization [34,41]. Scanning tunneling spectroscopy on bubblelike deformations see this quantization, where the observed pseudo-Landau levels correspond to PMFs stronger than 300 T [38,51].

Deformations can be induced in graphene samples by different techniques like pressurizing suspended graphene [36,52] or by exploiting the thermal expansion coefficients of different substrates [38]. As a result, introducing nonuniform strain distributions at the nanoscale is a promising way of realizing strain engineering. The standard theoretical approach to treat strain effects employs continuum mechanics to obtain the strain field. Several studies improve the accuracy by replacing the continuum mechanics with classical molecular dynamics simulations [6,36,37]. The strain field can then be coupled to an effective Dirac model of graphene to study the generation of PMFs in various geometries. In most studies, only the PMF distribution is considered as opposed to experimentally observable quantities like LDOSs. The framework presented in Sec. II enables us to treat the effect of strain on the LDOS directly from a tight-binding Hamiltonian. Consequently, we are now able to describe a single bubble in an extended system without applying periodic boundary conditions which may introduce interactions between neighboring bubbles. The dual recursive sweep then allows for efficient calculation of local properties everywhere in the device region surrounding a bubble, enabling us to investigate spatial variations in real-space LDOS maps. In this section we only treat one
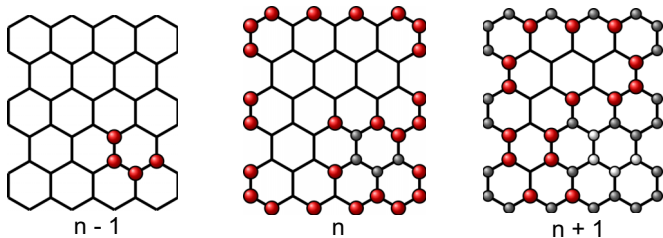

FIG. 4. (Color online) An example of the partitioning when the cell $n - 1$ is connected to the edge, and we need to include the boundary self-energy, Σ_B. In this case, all edge sites and self-energy terms are included in cell n. The symbols are similar to those in Fig. 3.

nanostructure, but the patched GF technique efficiently handles several spatially separated nanostructures, as the separation is added very efficiently through the self-energy term.

To account for strain within a tight-binding approach, we modify the hopping parameters [39,43,46]. The nearest-neighbor hopping in Eq. (6) between sites i and j is given by the new distance, d_{ij}, between the sites,

$$t_{ij} = t\, e^{-\beta\left(\frac{d_{ij}}{a_0} - 1\right)}, \qquad (12)$$

where the coefficient $\beta = -\partial \ln t / \partial \ln a_0 \approx 3.37$ [43]. We treat the deformation problem by applying an analytical displacement profile $[u(x,y), z(x,y)]$ matched against experimental data for pressurized suspended graphene [53]. Here $u(x,y)$ and $z(x,y)$ are the in-plane and vertical displacements, respectively, which are induced by the applied strain. For a rotationally symmetric aperture with radius R, these are given, in spherical coordinates (r,θ), as

$$z(r,\theta) = h_0 \left(1 - \frac{r^2}{R^2} \right), \qquad (13a)$$

$$u(r,\theta) = u_0 \frac{r}{R} \left(1 - \frac{r}{R} \right), \qquad (13b)$$

for $r < R$. Here h_0 is the maximal height of the bubble and $u_0 = 1.136 h_0^2 / R$ is a constant relating the out-of-plane and in-plane deformations [53]. We note that this profile gives rise to a sharp edge at $r = R$, and many of the features we discuss below emerge from the strongly clamped nature of this bubble type.

As shown in B, rotational symmetric strain profiles give rise to threefold symmetric PMFs in the effective Dirac model. This is shown in Fig. 5(a) for the strain profile considered in Eq. (13). As discussed in earlier studies [39,46,54], we get an asymmetric sublattice occupancy such that the LDOS of each sublattice has a threefold symmetric distribution following the PMF while rotated 60° compared to the opposite sublattice. In all calculations below, we therefore show only one sublattice because the result for the opposite sublattice can be obtained by a 60° rotation and the total pattern is a superposition of both [35,40].

Comparing the PMF distribution in Fig. 5(a) with the calculated LDOS maps at different energies in Figs. 5(b)–5(d) for a bubble of radius $R = 10$ nm and height $h_0 = 3$ nm, we immediately notice that the threefold symmetry is also present in the LDOS maps. However, the spatial LDOS maps have significant additional details compared to the PMF distribution.

In Fig. 6 we calculate the energy-dependent LDOS at the positions indicated by symbols (square, circle and triangle) in Fig. 5. We first consider the average of the LDOS within the "slice" containing the symbols, shown by the bottom (red) curve in Fig. 6. Two distinct oscillation types are observed, and we argue that these can be divided into Friedel-type and PMF-induced features. At high energies in particular we notice regularly spaced oscillations with an approximate period of $\hbar v_F \pi / 2R$. These are consistent with Friedel-type oscillations related to the size of the structure and emerging from interferences between electrons scattered at opposite sides of the bubble. An exact treatment needs to take into
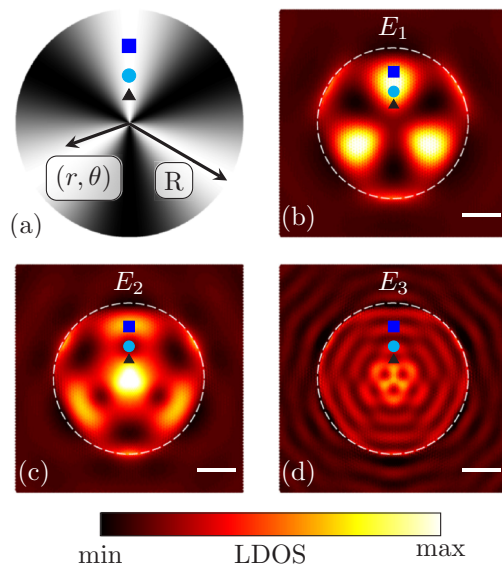

FIG. 5. (Color online) (a) The PMF distribution calculated using the strain distribution in Eq. (13), dark being negative field and light being positive. (b)–(d) Real-space LDOS maps for the A sublattice taken at the energies $E_1 = 0.06|t|$, $E_2 = 0.089|t|$, and $E_3 = 0.23|t|$, corresponding to energies of the first two pseudo-Landau levels and an energy dominated by Friedel-type oscillations, respectively. The energies and the symbols correspond the ones used in Fig. 6. Sublattice B is similar and is obtained by rotating 60°. The scale bar is 5 nm.

account the renormalized Fermi velocity, v_F, due to the average change in bond length [55]. At lower energies we observe distinct peaks which are not equally spaced (the first two appear at E_1 and E_2). We show that these are due to pseudomagnetic effects and we refer to them as pseudo-Landau levels.

Besides the Friedel oscillation associated with the bubble radius, we also have similar oscillations associated with the distances to different edges of the bubble. These features are highly position dependent and explain the differences between the three single-position curves in Fig. 6. When considering the average, these position-dependent oscillations are washed out
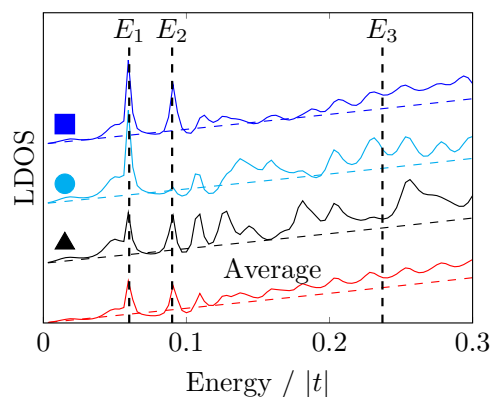

FIG. 6. (Color online) The LDOS as a function of energy for the three positions indicated in Fig. 5 and for the average of the "slice" of the bubble region containing the symbols. The dashed lines indicate the LDOS without the bubble. The curves are shifted with respect to each other to increase visibility.

(bottom curve in Fig. 6), leaving only the oscillation dependent on the structure size. However, at individual positions these oscillations can have a considerable impact. Returning to the individual position STS curves in Fig. 6, we note that the peak at E_2 is only dominant for the points indicated by the square and the triangle. It is suppressed by Friedel-type interferences at the circle point, which is also clear from the LDOS map in Fig. 5(c).

The amplitude of the Friedel-type oscillations is determined by the strength of scattering near the bubble edges. The clamped edge implied by the strength profile in Eq. (13) gives rise to significant strain fields along this edge, leading to a sharp, strong perturbation. More realistic profiles calculated from molecular dynamics also indicate strong perturbations near the edges of clamped bubbles [36]. Our results indicate that edge scattering effects may significantly affect LDOS behavior in clamped bubble systems and even mask PMF-induced features.

To treat the oscillations due to the feature size and edge sharpness in more detail, we calculate the LDOS for an artificial system only taking into account the strain field along a small ring around the edge; see Fig. 7 (dashed red line). In this way, only Friedel-type features are expected within the structure. If we compare to the full calculation (solid black line in Fig. 7), we notice that the oscillations at higher energies are present in both calculations, whereas the sharp peaks are only present in the full calculation. This confirms the Friedel nature of the higher energy oscillations and suggests that the lower energy peaks are due to an alternative mechanism. To confirm that the sharp peaks are due to pseudomagnetic effects, we compare the peak positions to the standard form expected for Landau levels in graphene $E_n = \text{sgn}(n)\sqrt{2e_0\hbar v_F^2 B_s n}$, where e_0 is the electron charge, B_s is the magnetic field, and n is the peak number [8]. The peaks labeled 1–4 in Fig. 7 display the $\sqrt{n}$-dependence characteristic of Landau levels in graphene, as shown in the inset of Fig. 7. The size of the PMF can furthermore be inferred to be $B_s \sim 30$ T from the inset.
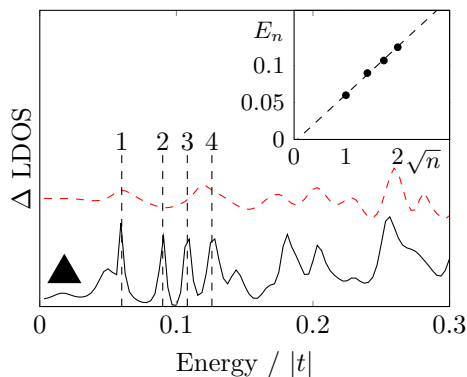

FIG. 7. (Color online) The difference in LDOS as a function of energy for the point indicated with a triangle on Fig. 5. We show both the full calculation (solid line) and an artificial system containing only the perturbation for a small region at the edge of the bubble (dashed line). We adjust the average hopping constant in the calculation of the artificial system to match the full calculation. (Inset) The peak energies 1–4 as a function of $\sqrt{n}$, where n is the peak number.

To conclude, we discussed how the features in the LDOS spectra of clamped graphene bubbles can be explained by a combination of size-dependent scattering and PMF-induced effects like pseudo-Landau quantization. Significant strain fields near the edge of the structure give rise to strong Friedel-type oscillations in the LDOS and these oscillations envelop the effect of a PMF. We must therefore be careful to distinguish between the two types of oscillations when investigating the electronic effects of PMFs induced by inhomogeneous strain fields.

IV. VORTEX CURRENTS NEAR PERFORATIONS

In this section we investigate local transport properties near antidots (i.e., perforations) in a graphene sheet. Periodic arrays of antidots have been studied as a way to open a band gap in graphene [56–58] or to obtain waveguiding effects [59,60]. Furthermore, a single perforation in a graphene sheet has been considered as a nanopore for DNA sensing [61,62] and recent studies in magnetic fields have shown the Aharonov-Bohm effect appearing in conducting edge states around a nanohole [63].

Several studies show that the electronic structure of antidots is closely related to the exact edge geometry [56,60,64]. Experimental fabrication techniques like block copolymer [3,4,65] or electron beam lithography [66–68] inevitably lead to disorder and imperfect edges. However, it may be possible to control the edge geometry of the antidot by heat treatment [67,69] or selective etching [68,70].

Motivated by the interest in how current flows in antidot systems, we apply the patched GF method to a single perforation in a graphene sheet. The method allows us to study the perforation with no influence from periodic repetition or finite sample size. Additionally, the combination of recursive methods and a boundary self-energy allows for the investigation of antidot sizes realizable experimentally [3,62,71]. In fact, we consider both an example antidot with perfect edges and an exact structure found from high-resolution transmission electron microscope (TEM) images using pattern recognition [72,73].

To investigate current on the nanoscale, recent experiments have realized multiple STM systems [15,16,74,75]. These allow for individual manipulation of several STM tips in order to make electrical contact to the sample near the considered nanostructure. Theoretically, we previously considered multiple STM setups allowing for both fixed and scanning probes [18,64]. The method presented here allows for not only transmission calculations but also calculation of local electronic and transport properties in the presence of multiple point probes. At the same time large separations between the different probes and/or nanostructures are easily included as additional separation is achieved in a very computationally efficient manner through the self-energy term connecting multiple patches. The combination of large spatial separation between features, while still enabling calculation of local electronic and transport properties, can prove to be a useful tool in investigating extended two-dimensional systems where we take special interest in a particular region of the extended sample.

In order to consider transmissions and current patterns, we add leads to the system through inclusion of a lead
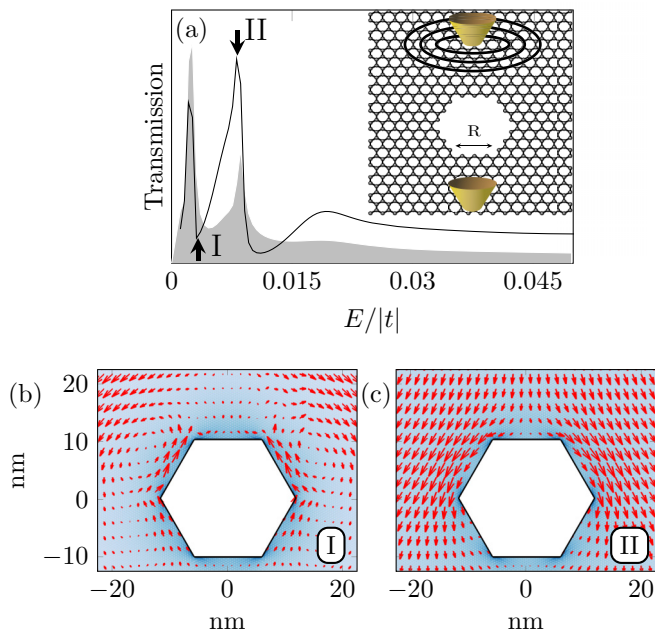
FIG. 8. (Color online) (a) The transmission as a function of energy for a dual probe setup with an antidot in between the probes as schematically shown in the inset. The distance between the probes is 200 nm and the antidot with purely zigzag edges has side length $R = 48a_0 \sim 6.8$ nm. The shaded area corresponds to the LDOS around the edge of the antidot.

self-energy term, $\Sigma_{ij}^L = V_{is}^L g^s(\mathbf{r}_i - \mathbf{r}_j)V_{sj}^L$, where V_{is}^L is the coupling element between the device site i and the lead. To model the structureless lead, we use the surface GF of a single atomic chain, because this has a constant DOS in the considered energy range. The distance dependence in $g^s(\mathbf{r}_i - \mathbf{r}_j)$ is necessary to avoid an unphysical coupling between different lattice sites via the lead. We therefore add a $1/|\mathbf{r}_i - \mathbf{r}_j|$ dependence for the off-diagonal terms [76], where $\mathbf{r}_i \neq \mathbf{r}_j$, as appropriate for a structureless three-dimensional free electron gas [77].

First, we consider a zigzag-edged antidot with side length $R = 48a \sim 12$ nm, where a is the length of the graphene unit cell and $a = \sqrt{3}a_0 = 2.46$ Å. This is comparable to experimental sizes where sub-20-nm feature sizes have been reported [3,4,62,65]. The antidot is between two probes placed 200 nm apart, as shown schematically in the inset of Fig. 8(a). The main panel of Fig. 8(a) shows the transmission as a function of energy for this dual point probe setup. We note the distinct transmission peaks. As explained in Ref. [64], these peaks are related to localized states along the zigzag edges. As a consequence, we notice the correspondence between the peaks in the transmission and the peaks in the LDOS around the edge; see the shaded area in Fig. 8(a).

Next, we calculate the bond currents from the top lead. The bond current between sites i and j from lead L are calculated, as explained in Appendix A, by $J_{ij}^L = -H_{ij}\text{Im}[\mathbf{G}^a\mathbf{\Gamma}^L\mathbf{G}^r]_{ij}/\hbar$, where H_{ij} is the Hamiltonian matrix element connecting sites i and j. The bond currents around the zigzag antidot for the energies indicated in Fig. 8(a) are shown in Figs. 8(b) and 8(c). In this way, we see that the transmission dips are related to vortexlike current paths. These vortex paths create a larger
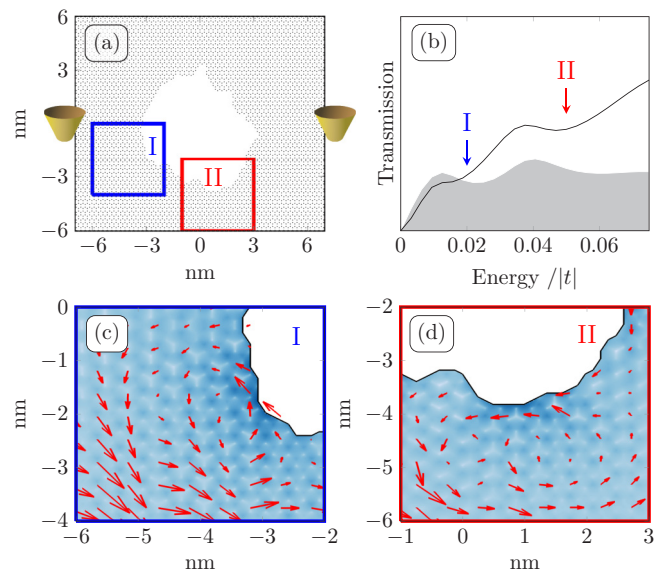

FIG. 9. (Color online) An actual perforation is obtained from high-resolution TEM images through pattern recognition and we consider the vortexlike current paths forming around the perforation as certain energies. (a) The structure of the perforation as well as an indication of the probe position (in the actual calculations the probes are 200 nm apart). The indicated areas correspond to the magnifications in (c) and (d). (b) The transmission for the dual probe setup. The shaded area indicates the average LDOS around the edge of the antidot. Furthermore, the energies I and II correspond to the energies used in (c) and (d), respectively. (c),(d) Bond current maps taken at the energies I and II, respectively, and shown at the positions indicated on (a).

"effective size" for the antidot at this energy, characterized by a region around the antidot avoided by the current paths. On the other hand, at the transmission peaks the current passes near the antidot edge.

The antidot considered in Fig. 8, although of realistic size, is an idealization, because experimental perforations will inevitably contain imperfections. To consider a more realistic case, we turn to a perforation observed in experimental TEM images. Using pattern recognition [72,73] the positions of the individual carbon atoms are obtained from high-resolution TEM images (see Fig. 9 of Ref. [73]). Pristine graphene is added around the experimentally obtained perforation to obtain the system shown in Fig. 9(a). From the transmission [see Fig. 9(b)], we notice that peaks are still present, but broadened by the disorder. Considering the two energies I and II in Fig. 9(b) and comparing their spatial current maps, we find that certain positions around the antidot are responsible for the additional backscattering causing the transmission dips. Dip I corresponds to a vortex pattern at the left side of the antidot [see Fig. 9(c)], whereas the dip at II is caused by a vortex pattern at the bottom of the antidot [see Fig. 9(d)]. This result suggests that electrons at different energies see a different effective perforation size and shape and are scattered accordingly.

V. CONCLUSION

We have expanded the standard RGF method to calculate local and transport properties enabling calculations in extended

nonperiodic systems. We exploit an efficient calculation of the pristine two-dimensional GF using complex contour methods. Once calculated, the pristine GFs are used to determine a boundary self-energy term describing the extended system. In this way, we can treat a finite device region embedded within an extended sample.

We first demonstrated how this approach is able to efficiently treat the electronic properties of strained bubbles in an extended graphene sheet. Considering a clamped bubble, we have shown that the finite size gives rise to Friedel-type oscillations in the density of states. This effect mixes with any pseudomagnetic effects arising from the strain field. We show that the edge effects can cloud pseudomagnetic signatures in the LDOS by adding additional structure which is not directly related to pseudomagnetic effects.

Second, we showed how finite leads can be added to a patched device region to efficiently calculate transport properties for spatially separated features, while still being able to map local properties in various parts of the system. In particular, we investigated the current flow around perforations of a graphene lattice. Both idealized geometries and experimental geometries obtained from high-resolution TEM images were considered. The transmissions show distinct dips caused by localized states along zigzag segments of the perforations. The transmission dips were associated with vortexlike current paths formed near the perforation edges.

We have demonstrated the versatility of this approach to the popular recursive GF method. The method allows for calculation of the same local and transport properties as standard methods, but adds the ability to treat large nonperiodic structures embedded in extended samples. We can extend the present method beyond nearest neighbor and to relevant alloys like hBN or transition-metal dichalcogenides. We therefore predict that the patched GF method will prove

to be a valuable tool in the investigation of nanostructures in two-dimensional materials.

APPENDIX A: RECURSIVE ALGORITHM

To obtain a tridiagonal Hamiltonian we let cell $n = 1$ contain all sites of interest. Then following the algorithm outlined below we assign all sites into cells.

(1) Let $\{n\}$ denote all sites in cell n and {"unassigned"} denote all sites not yet assigned to a cell.

(2) Find all sites j for which $H_{nj} \neq 0$, where $n \in \{n\}$ and $j \in$ {"unassigned"}. Denote these sites $\{n + 1\}$.

(2a) If $\{n + 1\}$ contains an edge site, then all remaining edge sites are added to $\{n + 1\}$.

(3) Sites in $\{n + 1\}$ are removed from {"unassigned"}

(4) Repeat 1–3 until all sites are assigned to a cell.

Step 2a is included if we require an edge self-energy term Σ_B as described in Sec. II.

Assuming the block tridiagonal partitioning obtained from the algorithm above, we make an update sweep starting from cell $n = N$, as shown schematically in Fig. 10. The steps are
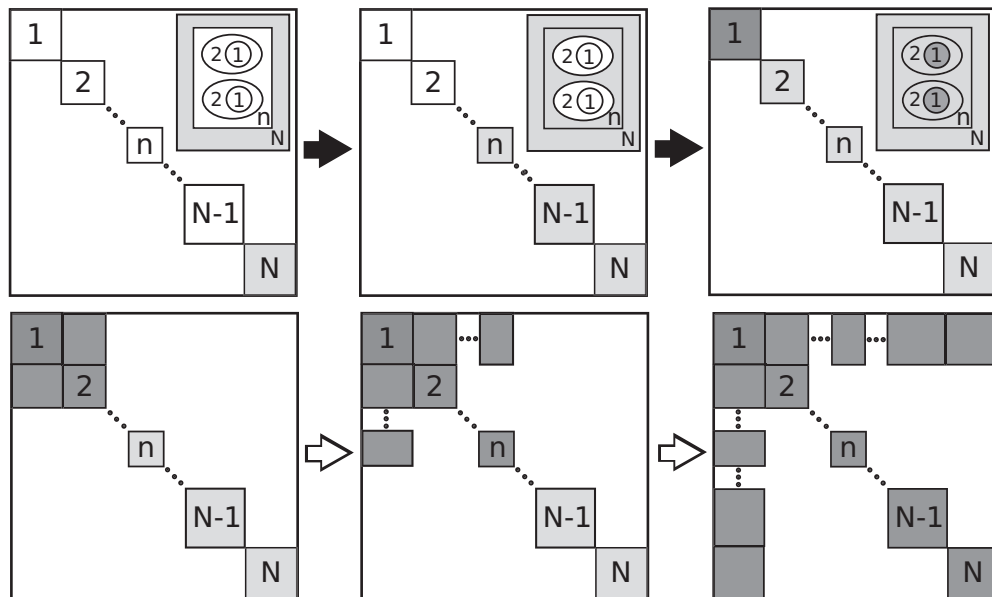

FIG. 10. (Top row) Recursive sweep going from cell $n = N$ to cell $n = 1$. Light gray indicates blocks that are stored for the reversed sweep and dark gray indicates blocks of the full GF. The insets show illustrations of how the different blocks correspond to neighboring cells in the device region. (Bottom row) Reversed recursive sweep going from $n = 1$ to $n = N$ showing how this sweep can obtain both diagonal and off-diagonal blocks.

calculated using the recursive relations [9]

$$g_{N,N} = (E - H_{N,N})^{-1}, \tag{A1a}$$

$$g_{n,n} = (E - H_{n,n} - V_{n,n+1}g_{n+1,n+1}V_{n+1,n})^{-1}, \tag{A1b}$$

$$g_{1,1} = \left(E - H_{1,1} - V_{1,2}g_{2,2}V_{2,1} - \sum_{m=1}^{M} \Sigma_{\text{lead}}^{m}\right)^{-1}, \tag{A1c}$$

where one of the $H_{n,n}$ terms includes the self-energy and Σ_{lead}^{m} terms are included if we calculate transmission. After the sweep is complete, the fully connected GF of cell $n = 1$ is obtained as $G_{1,1} = g_{1,1}$. As all sites of interest are placed in this cell, we can now calculate observables involving these sites. For example, we calculate transmission, $\mathcal{T}_{L,L'}$, between lead L and L' using these GFs,

$$\mathcal{T}_{L,L'}(E) = \text{Tr}\big[G_{L',L}\Gamma_{L,L}^{L}G_{L,L'}^{\dagger}\Gamma_{L',L'}^{L'}\big], \tag{A2}$$

where $\Gamma^{L} = i(\Sigma^{L} - \Sigma^{L\dagger})$ and $G_{L,L'}$ $(G_{L,L'}^{\dagger})$ is the retarded (advanced) GF connecting the two leads L and L'.

In order to obtain other blocks of the full GF matrix, we need to store the GF matrix, $g_{n,n}$, for each cell as we sweep from $n = N$ to $n = 1$. The stored blocks are shown in light gray in Fig. 10.

To obtain the LDOS at site i, $\rho_{ii} = -\text{Im}(G_{ii})/\pi$, we need the diagonal of the GF matrix. We calculate the block diagonal from a reversed sweep from $n = 1$ to $n = N$; see Fig. 10. The reversed sweep uses the block diagonals, $g_{n,n}$, from the first sweep to calculate the full diagonal GF, G,

$$G_{n,n} = g_{n,n} + g_{n,n}V_{n,n-1}G_{n-1,n-1}V_{n-1,n}g_{n,n}. \tag{A3}$$

Finally, we want to obtain bond currents for the state leaving a lead L. This can be calculated by $J_{ij}^{L} = -H_{ij}\text{Im}[G_{i,1}\Gamma_{1,1}^{L}G_{1,j}^{\dagger}]/\hbar$. Remembering that the leads are assigned to cell $n = 1$, we need the off-diagonal blocks, $G_{1,n}$ and $G_{n,1}$, in order to obtain bond currents. Using the stored GFs from the first sweep we can calculate the needed off-diagonals,

$$G_{1,n} = G_{1,n-1}V_{n-1,n}g_{n,n}, \tag{A4a}$$

$$G_{n,1} = g_{n,n}V_{n,n-1}G_{n-1,n}. \tag{A4b}$$

APPENDIX B: PSEUDOMAGNETIC FIELD FOR ROTATIONAL SYMMETRIC STRAIN FIELD

The strain tensor is generally given as

$$\epsilon_{ij} = \tfrac{1}{2}[\partial_{j}u_{i} + \partial_{i}u_{j} + (\partial_{i}z)(\partial_{j}z)], \quad i,j = x,y, \tag{B1}$$

where $u(x,y)$ is the in-plane deformation field and $z(x,y)$ is the out-of-plane deformation [50].

A general two-dimensional strain field, $\epsilon_{ij}(x,y)$, leads to a gauge field in the effective Dirac Hamiltonian of graphene [49,50],

$$A = -\frac{\hbar\beta}{2ea_{0}}\begin{pmatrix} \epsilon_{xx} - \epsilon_{yy} \\ -2\epsilon_{xy} \end{pmatrix}, \tag{B2}$$

which, in turn, gives a PMF,

$$B_{s} = \nabla \times A = \partial_{x}A_{y} - \partial_{y}A_{x}. \tag{B3}$$

Equations (B2) and (B3) imply that the x axis is chosen along the zigzag direction of the graphene lattice.

Now restricting ourselves to rotationally symmetric deformations, $u(r) = u_{r}$ and $z(r) = z$, while using polar coordinates (r,θ) yields

$$B_{s} = -\frac{\hbar\beta}{2ea_{0}}\left[2\frac{g(r)}{r} - \partial_{r}g(r)\right]\sin(3\theta), \tag{B4}$$

with $g(r) = \partial_{r}u_{r} - u_{r}/r + \frac{1}{2}(\partial_{r}z)^{2}$. We notice from Eq. (B4) that the PMF for a rotationally symmetric displacement field is always sixfold symmetric. On the other hand, the magnitude depends on both the in-plane and the out-of-plane displacements.

Considering the displacement field in Eq. (13), we now obtain a PMF of the form

$$B_{s} = -\frac{\hbar\beta u_{0}}{2ea_{0}R^{2}}\sin(3\theta). \tag{B5}$$

Taking into account the scaling $u_{0} \propto h_{0}^{2}/R$, we obtain a final scaling of the PMF with the size of the bubble $B_{s} \propto h_{0}^{2}/R^{3}$.

---

[1] A. K. Geim and I. V. Grigorieva, Nature (London) **499**, 419 (2013).

[2] G. Fiori, F. Bonaccorso, G. Iannaccone, T. Palacios, D. Neumaier, A. Seabaugh, S. K. Banerjee, and L. Colombo, Nat. Nanotechnol. **9**, 768 (2014).

[3] J. Bai, X. Zhong, S. Jiang, Y. Huang, and X. Duan, Nat. Nanotechnol. **5**, 190 (2010).

[4] M. Kim, N. S. Safron, E. Han, M. S. Arnold, and P. Gopalan, Nano Lett. **10**, 1125 (2010).

[5] F. Schedin, A. K. Geim, S. V. Morozov, E. W. Hill, P. Blake, M. I. Katsnelson, and K. S. Novoselov, Nat. Mater. **6**, 652 (2007).

[6] Z. Qi, D. A. Bahamon, V. M. Pereira, H. S. Park, D. K. Campbell, and A. H. C. Neto, Nano Lett. **13**, 2692 (2013).

[7] K. S. Novoselov and A. H. Castro Neto, Phys. Scr. T **146**, 014006 (2012).

[8] A. H. Castro Neto, N. M. R. Peres, K. S. Novoselov, and A. K. Geim, Rev. Mod. Phys. **81**, 109 (2009).

[9] C. Lewenkopf and E. Mucciolo, J. Comput. Electron. **12**, 203 (2013).

[10] S. Datta, *Electronic Transport in Mesoscopic Systems* (Cambridge University Press, Cambridge, UK, 1997).

[11] L. E. F. Foa Torres, S. Roche, and J.-C. Charlier, *Introduction to Graphene-Based Nanomaterials* (Cambridge University Press, Cambridge, UK, 2014).

[12] K. Kazymyrenko and X. Waintal, Phys. Rev. B **77**, 115119 (2008).

[13] M. Wimmer and K. Richter, J. Comput. Phys. **228**, 8548 (2009).

[14] C. W. Groth, M. Wimmer, A. R. Akhmerov, and X. Waintal, New J. Phys. **16**, 063065 (2014).

[15] J. Baringhaus, M. Ruan, F. Edler, A. Tejeda, M. Sicot, A.-P. Li, Z. Jiang, E. H. Conrad, C. Berger, C. Tegenkamp, and W. A. de Heer, Nature (London) **506**, 349 (2014).

[16] P. W. Sutter, J.-I. Flege, and E. A. Sutter, Nat. Mater. **7**, 406 (2008).

[17] F. R. Eder, J. Kotakoski, K. Holzweber, C. Mangler, V. Skakalova, and J. C. Meyer, Nano Lett. **13**, 1934 (2013).

[18] M. Settnes, S. R. Power, D. H. Petersen, and A.-P. Jauho, Phys. Rev. Lett. **112**, 096801 (2014).

[19] S. R. Power and M. S. Ferreira, Phys. Rev. B **83**, 155432 (2011).

[20] R. N. Sajjad, C. A. Polanco, and A. W. Ghosh, J. Comput. Electron. **12**, 232 (2013).

[21] C. Bena, Phys. Rev. B **79**, 125427 (2009).

[22] J. A. Lawlor and M. S. Ferreira, Physica B: Condens. Matter **463**, 48 (2015).

[23] S. R. Power, P. D. Gorman, J. M. Duffy, and M. S. Ferreira, Phys. Rev. B **86**, 195423 (2012).

[24] M.-H. Liu, P. Rickhaus, P. Makk, E. Tóvári, R. Maurand, F. Tkatschenko, M. Weiss, C. Schönenberger, and K. Richter, Phys. Rev. Lett. **114**, 036601 (2015).

[25] D. A. Areshkin and B. K. Nikolić, Phys. Rev. B **81**, 155450 (2010).

[26] M. Yang, X.-J. Ran, Y. Cui, and R.-Q. Wang, Chin. Phys. B **20**, 097201 (2011).

[27] G. Thorgilsson, G. Viktorsson, and S. Erlingsson, J. Comput. Phys. **261**, 256 (2014).

[28] G. Metalidis and P. Bruno, Phys. Rev. B **72**, 235304 (2005).

[29] A. Cresti, R. Farchioni, G. Grosso, and G. P. Parravicini, Phys. Rev. B **68**, 075306 (2003).

[30] E. Costa Girão and V. Meunier, J. Comput. Electron. **12**, 123 (2013).

[31] F. Libisch, S. Rotter, and J. Burgdörfer, New J. Phys. **14**, 123006 (2012).

[32] P. Drouvelis, P. Schmelcher, and P. Bastian, J. Comput. Phys. **215**, 741 (2006).

[33] T. Low, F. Guinea, and M. I. Katsnelson, Phys. Rev. B **83**, 195436 (2011).

[34] F. Guinea, M. I. Katsnelson, and A. K. Geim, Nat. Phys. **6**, 30 (2009).

[35] G. W. Jones and V. M. Pereira, New J. Phys. **16**, 093044 (2014).

[36] Z. Qi, A. L. Kitt, H. S. Park, V. M. Pereira, D. K. Campbell, and A. H. Castro Neto, Phys. Rev. B **90**, 125419 (2014).

[37] M. Neek-Amal and F. M. Peeters, Phys. Rev. B **85**, 195445 (2012).

[38] J. Lu, A. H. Castro Neto, and K. P. Loh, Nat. Commun. **3**, 823 (2012).

[39] R. Carrillo-Bastos, D. Faria, A. Latgé, F. Mireles, and N. Sandler, Phys. Rev. B **90**, 041411 (2014).

[40] F. D. Juan, A. Cortijo, M. A. H. Vozmediano, and A. Cano, Nat. Phys. **7**, 810 (2011).

[41] M. Neek-Amal, L. Covaci, K. Shakouri, and F. M. Peeters, Phys. Rev. B **88**, 115428 (2013).

[42] M. Neek-Amal and F. M. Peeters, Phys. Rev. B **85**, 195446 (2012).

[43] V. M. Pereira, A. H. Castro Neto, and N. M. R. Peres, Phys. Rev. B **80**, 045401 (2009).

[44] V. M. Pereira and A. H. Castro Neto, Phys. Rev. Lett. **103**, 046801 (2009).

[45] V. M. Pereira, R. M. Ribeiro, N. M. R. Peres, and A. H. Castro Neto, Europhys. Lett. **92**, 67001 (2010).

[46] D. Moldovan, M. Ramezani Masir, and F. M. Peeters, Phys. Rev. B **88**, 035446 (2013).

[47] F. M. D. Pellegrino, G. G. N. Angilella, and R. Pucci, Phys. Rev. B **81**, 035411 (2010).

[48] Z. H. Ni, T. Yu, Y. H. Lu, Y. Y. Wang, Y. P. Feng, and Z. X. Shen, ACS Nano **2**, 2301 (2008).

[49] H. Suzuura and T. Ando, Phys. Rev. B **65**, 235412 (2002).

[50] M. Vozmediano, M. Katsnelson, and F. Guinea, Phys. Rep. **496**, 109 (2010).

[51] N. Levy, S. A. Burke, K. L. Meaker, M. Panlasigui, A. Zettl, F. Guinea, A. H. Castro Neto, and M. F. Crommie, Science **329**, 544 (2010).

[52] J. S. Bunch, S. S. Verbridge, J. S. Alden, A. M. van der Zande, J. M. Parpia, H. G. Craighead, and P. L. McEuen, Nano Lett. **8**, 2458 (2008).

[53] K. Yue, W. Gao, R. Huang, and K. M. Liechti, J. Appl. Phys. **112**, 083512 (2012).

[54] M. Schneider, D. Faria, S. V. Kusminskiy, and N. Sandler, arXiv:1501.02981.

[55] F. M. D. Pellegrino, G. G. N. Angilella, and R. Pucci, Phys. Rev. B **84**, 195404 (2011).

[56] T. G. Pedersen, C. Flindt, J. G. Pedersen, N. A. Mortensen, A.-P. Jauho, and K. Pedersen, Phys. Rev. Lett. **100**, 136804 (2008).

[57] T. Gunst, T. Markussen, A.-P. Jauho, and M. Brandbyge, Phys. Rev. B **84**, 155449 (2011).

[58] J. A. Fürst, J. G. Pedersen, C. Flindt, N. A. Mortensen, M. Brandbyge, T. G. Pedersen, and A. P. Jauho, New J. Phys. **11**, 095020 (2009).

[59] J. G. Pedersen, T. Gunst, T. Markussen, and T. G. Pedersen, Phys. Rev. B **86**, 245410 (2012).

[60] S. R. Power and A.-P. Jauho, Phys. Rev. B **90**, 115408 (2014).

[61] G. F. Schneider, S. W. Kowalczyk, V. E. Calado, G. Pandraud, H. W. Zandbergen, L. M. K. Vandersypen, and C. Dekker, Nano Lett. **10**, 3163 (2010).

[62] C. A. Merchant, K. Healy, M. Wanunu, V. Ray, N. Peterman, J. Bartel, M. D. Fischbein, K. Venta, Z. Luo, A. T. C. Johnson, and M. Drndić, Nano Lett. **10**, 2915 (2010).

[63] Y. I. Latyshev, A. P. Orlov, V. A. Volkov, V. V. Enaldiev, I. V. Zagorodnev, O. F. Vyvenko, Y. V. Petrov, and P. Monceau, Sci. Rep. **4**, 7578 (2014).

[64] M. Settnes, S. R. Power, D. H. Petersen, and A.-P. Jauho, Phys. Rev. B **90**, 035440 (2014).

[65] M. Kim, N. S. Safron, E. Han, M. S. Arnold, and P. Gopalan, ACS Nano **6**, 9846 (2012).

[66] J. Eroms and D. Weiss, New J. Phys. **11**, 095021 (2009).

[67] Q. Xu, M.-Y. Wu, G. F. Schneider, L. Houben, S. K. Malladi, C. Dekker, E. Yucelen, R. E. Dunin-Borkowski, and H. W. Zandbergen, ACS Nano **7**, 1566 (2013).

[68] F. Oberhuber, S. Blien, S. Heydrich, F. Yaghobian, T. Korn, C. Schüller, C. Strunk, D. Weiss, and J. Eroms, Appl. Phys. Lett. **103**, 143111 (2013).

[69] X. Jia, M. Hofmann, V. Meunier, B. G. Sumpter, J. Campos-Delgado, J. M. Romo-Herrera, H. Son, Y.-P. Hsieh, A. Reina, J. Kong, M. Terrones, and M. S. Dresselhaus, Science **323**, 1701 (2009).

[70] F. Pizzocchero, M. Vanin, J. Kling, T. W. Hansen, K. W. Jacobsen, P. Bøggild, and T. J. Booth, J. Phys. Chem. C **118**, 4296 (2014).

[71] A. Cagliani, D. Mackenzie, L. Tschammer, F. Pizzocchero, K. Almdal, and P. Bøggild, Nano Res. **7**, 743 (2014).

[72] J. Kling, J. S. Vestergaard, A. B. Dahl, N. Stenger, T. J. Booth, P. Bøggild, R. Larsen, J. B. Wagner, and T. W. Hansen, Carbon **74**, 363 (2014).

[73] J. S. Vestergaard, J. Kling, A. B. Dahl, T. W. Hansen, J. B. Wagner, and R. Larsen, Microsc. Microanal. **20**, 1772 (2014).

[74] K. W. Clark, X.-G. Zhang, G. Gu, J. Park, G. He, R. M. Feenstra, and A.-P. Li, Phys. Rev. X **4**, 011021 (2014).

[75] A.-P. Li, K. W. Clark, X.-G. Zhang, and A. P. Baddorf, Adv. Funct. Mater. **23**, 2509 (2013).

[76] The surface GF of the single atomic chain is given by $g^s = \frac{E \pm \sqrt{E^2 - 4\gamma^2}}{2\gamma^2}$ [77]. We chose $\gamma = |t|$ as this gives a constant DOS within the considered energies. The distance dependence for off-diagonal finally gives the GF, $g^s(\boldsymbol{r}_i - \boldsymbol{r}_j) = \delta_{ij} g^s + (1 - \delta_{ij}) \frac{g^s}{|\boldsymbol{r}_i - \boldsymbol{r}_j|}$.

[77] E. N. Economou, *Green's Functions in Quantum Physics* (Springer, Berlin, 2005).